Effect of Laser Power on Corrosion Properties of Hybrid Welded 2195 Al-Li Alloy

Mei Yang[1], Honglang Yang[1], Lie Yang[2], Yang Liu[1], Jian Tan[3], Jin Chen[4]

[1] School of materials Science and Engineering, Southwest Petroleum University, Chengdu610500, China
[2] Pangang Group Engineering Consulting Co., Ltd, Panzhihua 617000, China
[3] Engineering Technology Research Institute, PetroChina Southwest Oil and Gas Field Company, Deyang618300, China
[4] Engineering and Technology Development Training Center of SPC, Chengdu 610213, China
[*]E-mail: meiyangs0099@163.com

In this work, the effect of laser power on corrosion properties of 2195 Al-Li alloy laser hybrid welded joints was investigated. The results show that with the laser power increases, the microstructure of the weld is coarsened, the amount of bright white and dark black precipitates decrease, the size of the precipitates increases and the distribution is nonuniform. Electrochemical test shows that the corrosion resistance of the base metal (BM) is lower than that of the heat-affected zone (HAZ), and the corrosion resistance of the weld is the highest among the areas considered herein. The corrosion resistance of the weld increases with increasing laser power. The result of inter-granular corrosion (IGC) testing shows that the HAZ has the best IGC resistance among the areas considered herein. The IGC analysis of the weld metals shows that the average and maximum depth of IGC decrease with increasing laser power. When the laser power reaches 1300 W, the average and maximum depths of inter-granular corrosion are 146 μm and 164 μm, respectively.

1. INTRODUCTION

The 2195 Al-Li alloy has good application potential in the aerospace industry due to its low density, high strength, good plasticity, good toughness and good corrosion resistance [1-4]. At present, research concerning the welding methods for Al-Li alloys mainly includes arc welding, laser welding and friction stir welding [5-7]. Compared with other welding methods, laser welding has the advantages of a small heat-affected zone (HAZ) and small welding deformation [8]. However, the microstructure and composition of the welded joints can be changed greatly during the laser welding

process, and the coating of aluminum on the joint surface can also be damaged, which deteriorates the corrosion performance of the welded joint [9-10]. Therefore, studying the corrosion performance of 2195 Al-Li alloy welded joints has practical significance for the safety implications.

Many studies have been conducted to investigate the corrosion performance of aluminium alloy welded joints. Work by Xu, et al [11] involved the microstructure and corrosion behaviour of nugget zones during friction stir welding of a 2219-O aluminium alloy. The results showed that Al_2Cu acted as a cathode and formed a couple with the Al matrix, which lead to the first dissolution of the Al. The corrosion behaviour of 2024-T3 aluminium alloy friction stir welded joints was studied by Bousquet, et al [12], and the results indicated that coarse precipitates were the origin of pitting corrosion. Because the S (Al_2CuMg) phase particles precipitated along grain boundaries in the HAZ, the inter-granular corrosion (ICG) sensitivity of HAZ was elevated. Proton, et al [13] studied the IGC sensitivity of a 2050-T3 aluminium alloy friction stir welded joint and observed that it was higher than that of the base metal (BM); the electrochemical test showed that the galvanic corrosion that was formed in the different regions of the joint may have affected the corrosion behaviour of the joint.

In this work, the corrosion resistance of a laser-arc hybrid welded 2195 Al-Li alloy was investigated at different laser powers. Relatively little research has been conducted on the corrosion resistance of this process. This work is of great significance for the safe use of 2195 Al-Li alloys in aerospace applications .

2. EXPERIMENTAL MATERIALS AND METHODS

Sheets comprising the 2195 Al-Li alloy with a thickness of 3 mm were received in the T8 condition. An ER4047 Al-Si filler wire with a diameter of 1.2 mm was used for the welding. The chemical composition of the filler wire and BM are given in Table 1 and Table 2.

Table 1. Chemical composition of the 2195 Al-Li alloy (wt.%)

Cu	Li	Mg	Ag	Zr	Fe	Al
4	1	0.44	0.4	0.11	0.05	Bal

Table 2. Chemical compositions of the Al-Si filler wire (wt.%)

Si	Mg	Fe	Cu	Zn	Mn	Al
12	≤0.10	≤0.80	≤0.03	≤0.20	≤0.15	Bal

The welded joints were manufactured by a hybrid-arc welding system consisting of a fibre laser (IPG YLS-4000-S2T-CL) and MAG welder (Kemp Arc Pulse 450). The 2195 Al-Li alloy plates were placed horizontally, and the assembly gap was 0.5 mm, which was fixed by a clamping device. The laser was perpendicular to the 2195 Al-Li alloy sheet and approximately 30° to the MAG arc. The two welding heat sources were combined to act on the 2195 Al-Li alloy to be welded. The shielding gas was dry pure argon gas. The welding parameters that were used are summarized in Table 3.

Table 3. The welding parameters of hybrid laser-arc welding

Laser power (W)	Wire feeding rate (mm/s)	Welding velocity (mm/s)	Welding current (A)	Welding voltage (V)
700	8	11.5	142	19
1000	8	11.5	143	19
1300	8	11.5	147	18.5

After welding, cross sections of the welds were cut with a wire-electrode from the joints that were welded with different laser powers. The welded joints were ground, polished and etched with Keller solution (HF: HCL: HNO$_3$: H$_2$O =2:3:5:190) for optical microscopy (OM, DME-300M). The microstructure of the weld cross sections was observed by scanning electron microscopy (SEM, FEI Quanta 650 FEG). Afterwards, the phase composition was determined by X-ray diffraction (XRD, X'Pert PRO MPD)

The electrochemical tests were carried out in a comprehensive electrochemical test system (PGSTAT 302N). The three-electrode cell consisted of a reference electrode (a saturated calomel electrode), an auxiliary electrode (a platinum plate) and a working electrode (samples under test). The test specimen was welded together with copper wire by tin welding, leaving an open area on the sample for measurement, the rest of the area was sealed with silica gel. During the test, the specimen was protected from oxidation due to exposure to the ambient air as much as possible. The solution used in the experiment was a sodium chloride aqueous solution with a mass fraction of 3.5%. The measurement time of the open circuit potential was 2000 s. The polarization was -0.3 V to 0.33 V and the scanning rate was 0.02 V/min.

The IGC tests were performed according to the IGC GB7998-2005 test standard. The corrosion solution was prepared with 57 g NaCl, 1 L H$_2$O and 10 ml H$_2$O$_2$ (ρ 1.10 g/ml). The corrosion time and temperature were 6 hours and 35°C±2°C, respectively. Before the corrosion test, the surface of the sample was polished and cleaned with acetone. After 6 hours, the samples were removed and rinsed gently with deionized water. The samples were dried with cold air. The surface corrosion of the specimen was observed with a stereomicroscope. Then the cross section of the weld was ground with sand-paper and polished, the corrosion depth was then measured with an optical microscope.

3. RESULTS AND DISCUSSION

3.1 Microstructure of the weld joints

Fig.1 shows the microstructures of the weld metals that were produced with different laser powers. With an increase in the laser power from 700 W to 1300 W, the weld microstructures coarsen, dendrite spacing increases, and secondary dendrites become increasingly developed. Shu, et al [14] also found that the dendrite size increased simultaneously with increasing laser power. From the backscattering image, it can be seen that with increasing laser power, the amount of bright white and dark precipitates decreases, the size of the precipitates increases and the distribution is not uniform.
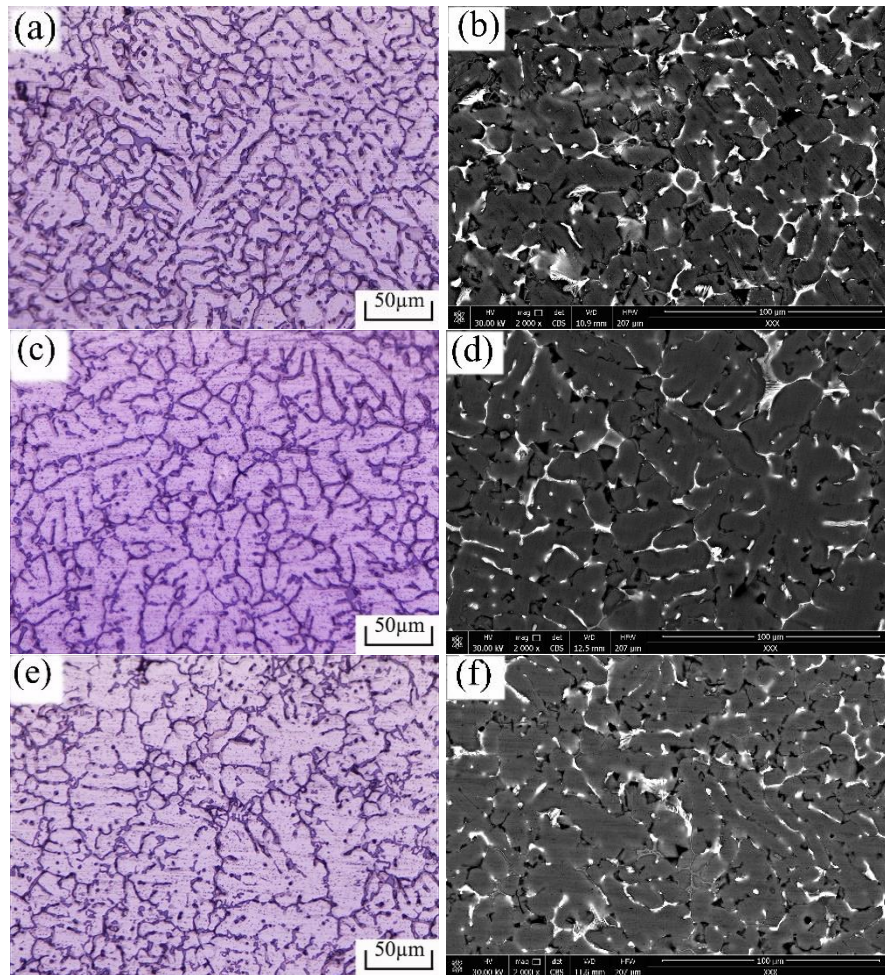
Figure 1. SEM micrographs of the microstructure of the weld metals produced with different laser powers. 700 W: (a) and (b), 1000 W: (c) and (d), 1300 W: (e) and (f)

The analysis shows that an increase in laser power leads to an increase in the welding heat input, and an increase in the residence time of the molten pool at high temperature, and an increase in the growth and coarsening of the grains. The coarsening of the grain structure leads to a decrease in the grain boundaries, and the second phase that precipitates along the the grain boundaries is large and nonuniform. With an increase in the laser power, the laser keyhole penetrates deeply into the bottom of the molten pool, the convection of the molten metal in the molten pool intensifies, and the segregation of alloying elements decreases, which leads to a decrease in the driving force of the second phase precipitation. Thus, the precipitated phase decreases, which is consistent with the second phase distribution in the backscattering image.
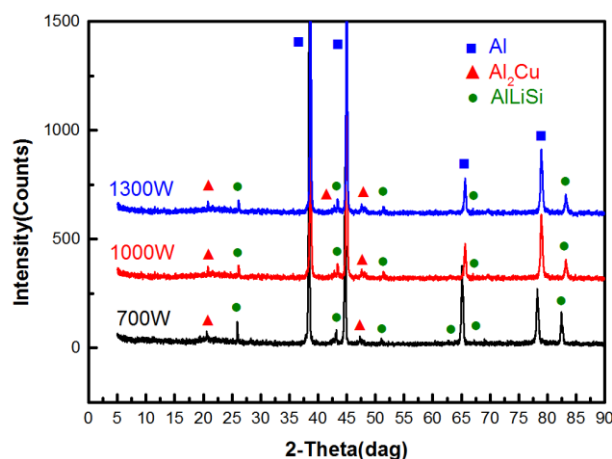
Figure 2. XRD diffraction spectra of the weld metals

The phase composition of the weld metals was analysed by X-ray diffraction, as shown in Fig.2. The main phases in the weld metals are α (Al), θ (Al$_2$Cu) and T (AlLiSi). The composite T (AlLiSi) and the θ (Al$_2$Cu) phases are the main strengthening phases in the weld when the laser arc is applied to the 2195 Al-Li alloy with an Al-Si welding wire. It is well known that the θ (Al$_2$Cu) phase is also the main strengthening phase in 2195 Al-Li alloys [15]. The presence of T (AlLiSi) is consistent with the previous observation in other Al-Li alloys produced by LBW [16].
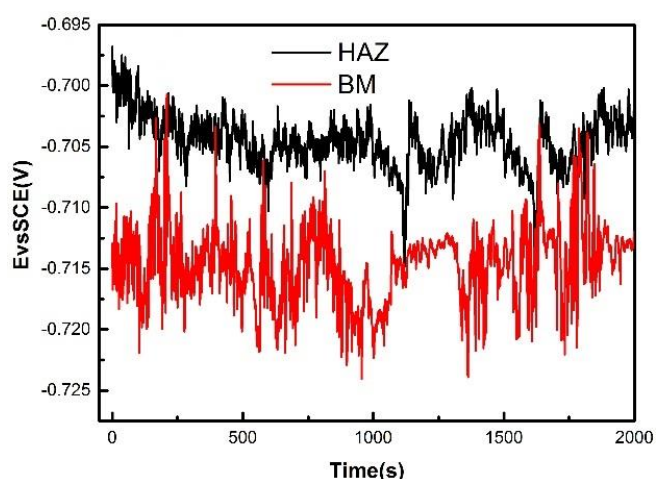
3.2 Electrochemistry measurements

Figure 3. Open-circuit potential (OCP) curves for the BM and HAZ in 3.5% NaCl solution

The open-circuit potential and polarization curves from the BM and HAZ are shown in Fig.3 and Fig.4, respectively. Table 4 lists the OCP, E$_{corr}$ and I$_{corr}$ for the BM and HAZ. It can be seen that the open-circuit potential curve of the HAZ is relatively stable, and above that of the BM. The stabilized electrode potential of the HAZ is -0.707 V, which is higher than the BM stabilized electrode potential value of -0.717 V. The fitting results of the polarization curves also show that the BM has a greater corrosion tendency than the HAZ.
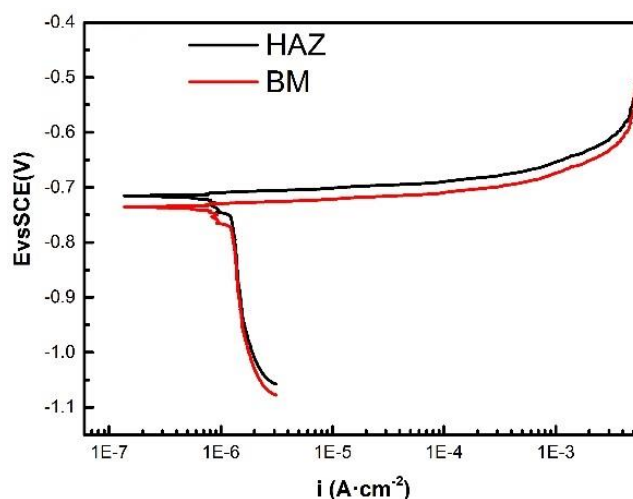
Figure 4. Polarization curves for the BM and HAZ in 3.5% NaCl solution

Table 4. Open circuit potential (OCP), corrosion potential E_{corr} and corrosion current density I_{corr} for the BM and HAZ

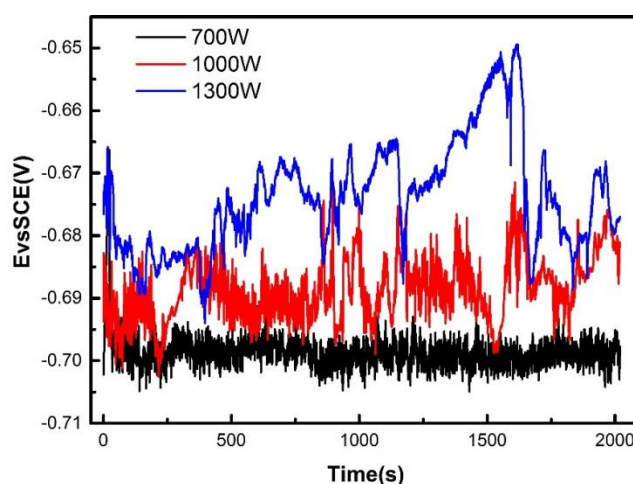| Position	OCP (V)	E_{corr} (V)	I_{corr} (A/cm^2)
HAZ	-0.707	-0.710	5.219×10^{-6}
BM	-0.717	-0.725	6.012×10^{-6}

Figure 5. Open-circuit potentials of weld metal produced with different laser powers in 3.5% NaCl solution

Relevant studies [17-18] show that the strengthening phase in the Al-Li alloy has high electrochemical activity, and couples readily with the surrounding Al matrix. The strengthening phase acts as a cathode, and the Al matrix acts as an anode, which leads to the dissolution of the Al matrix. In a corrosive environment (NaCl solution), the closed circuit is composed of a precipitated phase and a low potential aluminium matrix, which results in corrosion occurring first around the precipitated

phase. Therefore, the corrosion resistance of the weld is closely related to the amount of the precipitated phase. Some of the precipitates dissolve in the HAZ after thermal cycling, so there are fewer precipitates in the HAZ than in the BM. so the corrosion tendency of the HAZ is lower than that of the BM and higher than that of the weld metal.
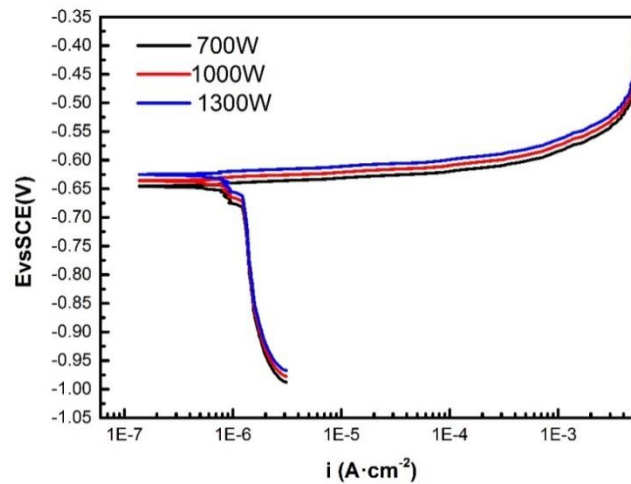

Figure 6. Polarization curves of weld metals produced with different laser powers in 3.5% NaCl solution

Table 5. Open circuit potential (OCP), corrosion potential E_{corr} and corrosion current density I_{corr} of weld metals produced with different welding powers

Laser power(W)	OCP (V)	E_{corr}(V)	I_{corr}(A/cm^2)
700	-0.699	-0.678	2.963×10^{-6}
1000	-0.686	-0.655	2.614×10^{-6}
1300	-0.674	-0.620	1.963×10^{-6}

Fig. 5 shows the open-circuit potentials of weld metals produced with different laser powers in 3.5% NaCl solution. Table 5 shows that OCPs at 700W, 1000W and 1300W are -0.699 V, -0.686 V and -0.674 V, respectively. Thus, as the laser power increases, the corrosion resistance of the weld metal increases.

Fig. 6 shows the polarization curves of the weld metals under different laser powers in a 3.5% NaCl solution. The polarization process of the anode involves active dissolution, and no passivation zones can be observed. The cathodic curve has a greater coincidence, which indicates that the cathodic polarization process is completely controlled by oxygen diffusion. Table 6 shows that as the laser power increases from 700 W to 1000 W to 1300 W, the corrosion potential increases from -0.678 V to -0.655 V to -0.620 V, and the corrosion current density decreases from 2.963×10^{-6} A/cm^2 to 2.614×10^{-6} A/cm^2 to 1.963×10^{-6} A/cm^2, respectively. As shown in Fig. 1, when the laser power increases the heat

input and the cooling rate of the molten pool decreases, the driving force for precipitation decreases, resulting in a decrease in the amount of precipitation. According to the description above, in a corrosive environment (NaCl solution), a closed circuit is formed by a precipitated phase and a low potential aluminium matrix, which leads to accelerated matrix corrosion. Therefore, as the laser power increases, the corrosion resistance of the weld metal increases.

3.3 IGC behaviours

Different areas of the welded joint are presented in Fig. 7. Severe inter-granular corrosion morphology is observed on the surface of the weld metal, in which the corrosion products delaminated due to severe corrosion. The cross-sectional morphology of the weld area shows that the depth of the inter-granular corrosion is not uniform. The corrosion that is generated and has expanded along the grain boundaries is presented in the magnified images of the cross-sectional morphology in Fig. 7. The severity of the corrosion in the HAZ is lower than that of the weld, and a small amount of corrosion products can be seen on the upper surface, but no obvious corrosion product is has delaminated. The cross-sectional morphology shows that the depth of the inter-granular corrosion in the HAZ is shallow. The BM contains corrosion that is peeling away, and the upper surface of the BM is severely corroded, and large corrosion pits are generated due to delamination of the corrosion products. The cross-sectional morphology indicates that the corrosion depth of the BM is greater than that of the HAZ and lower than that of the weld metal. Liu, et al [19] also found that the most severe corrosion occurred in the weld metal when they studied the corrosion resistance of a 2060 laser welded joint.
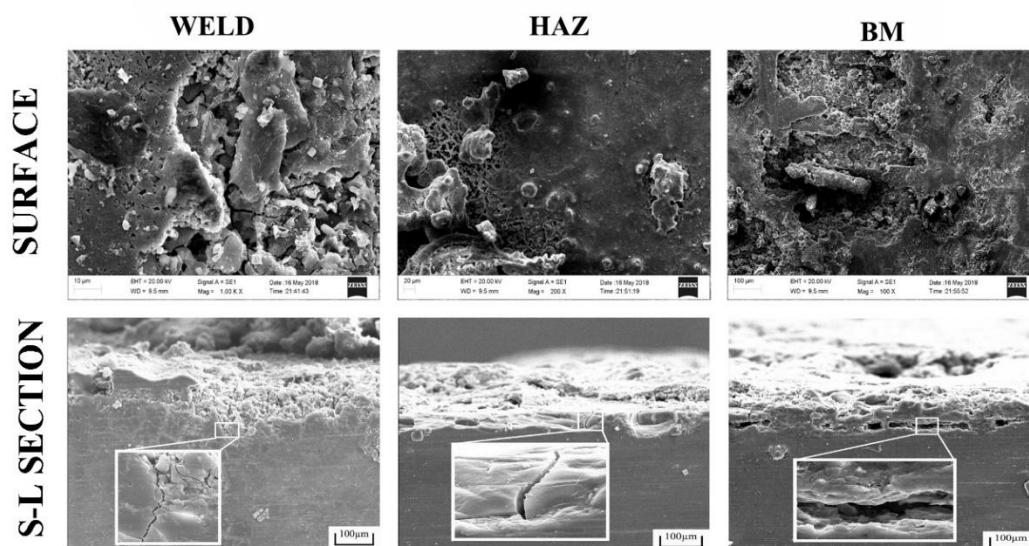

Figure 7. Morphology of IGC in different regions of the welded joints

Al-Li alloys usually depend on the precipitation of a strengthening phase to improve their performance. A large amount of T1 and θ phases are precipitated in the matrix, and distributed in dislocations, grain boundaries and subgrain boundaries. The electrochemical activity of the

precipitated phase is high, and the electrochemical activity of the T1 phase is much higher than that of the aluminum matrix [20]. The corrosion potential of the precipitated phase is high and a potential difference is formed with the surrounding matrix, resulting in an increase in the corrosion rate of the surrounding matrix [21]. Therefore, the amount and location of the strengthening phase may have a direct impact on the occurrence of corrosion.

The Al-Li alloy is subjected to heat treatment to obtain the super-saturation necessary for solid solution precipitation. Due to the severe distortion of the lattice and high energy at the dislocations, grain boundaries and subgrain boundaries, the strengthening phase is preferentially precipitated in the interior of the grains as much as possible to enhance the comprehensive mechanical properties of the BM. The BM is pre-deformed to increase the number of dislocations and subgrain boundaries within the grains. However, due to different Schmidt factors at different locations, the ability to plastically deform is different, and the number of dislocations and sub-grain boundaries in different regions is also different. In a region with an elevated Schmidt factor, the plastic deformation ability increases and the number of dislocations and sub-grain boundaries increases, which leads to additional precipitation of the strengthening phase. These location are preferentially corroded when exposed to an inter-granular corrosion solution [22-23], which could be attributed to the severe inter-granular corrosion in part of the BM.

A few corrosion products occur in HAZ and no obvious corrosion products delaminate from the upper surface, the overall corrosion degree is relatively uniform. The depth of the inter-granular corrosion is relatively shallow as seen in the cross section of the weld. Due to the thermal cycling during the welding process, some of the strengthening phases of HAZ are dissolved and remelted into the BM to form a supersaturated solid solution; some of the phases aggregate and grow, causing the amount of the overall strengthening phase decrease [24]. At the same time, a considerable portion of the precipitates in the HAZ are located at dislocations and sub-grain boundaries in the interior of the grains, and the grain boundary corrosion cannot be accelerated during the inter-granular corrosion process. Therefore, the corrosion severity in the HAZ is weak. In contrast to the precipitates in HAZ dispersed in the dislocations, sub-grain boundaries and grain boundaries, the precipitates in the weld zone are mainly located in the grain boundaries and a small amount are in the grain interiors[19]. A large amount of copper-rich precipitates at the grain boundaries and in the surrounding BM are prone to microscopic galvanic corrosion[25]. Therefore, the precipitates at the grain boundaries benefit the propagation of IGC along the grain boundaries, which increases the severity and depth of the IGC of the weld metal.
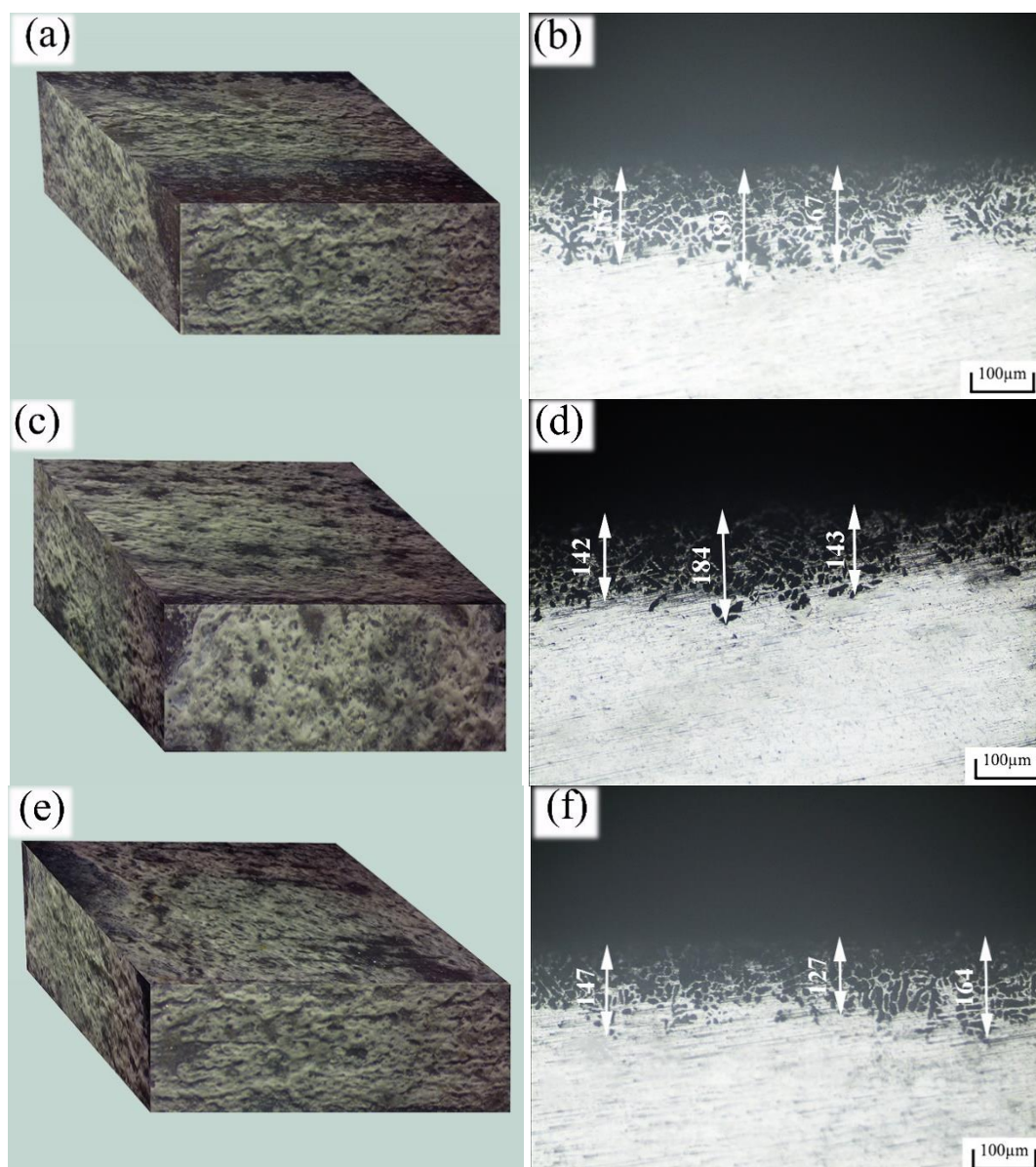
Figure 8. Morphology and depth of IGC of the weld metals produced with different laser powers. 700 W: (a) and (b), 1000 W: (c) and (d), 1300 W: (e) and (f)

Fig.8 shows the morphology of the IGC in the weld metal under different laser powers. The depth of the IGC in the cross section of the weld is measured at a magnification of 200 times in the optical microscope. The IGC samples are covered by a large amount of white corrosion products. The IGC gradually expands from the surface to the inside of the weld metal, and the corrosion spreads along the grain boundaries. The IGC depth of the weld metal under different laser powers was measured. To reflect the corrosion situation as far as possible, the corrosion depth at three different locations is determined as shown in Table 6.

Table 6. IGC depth of weld metal under different laser power

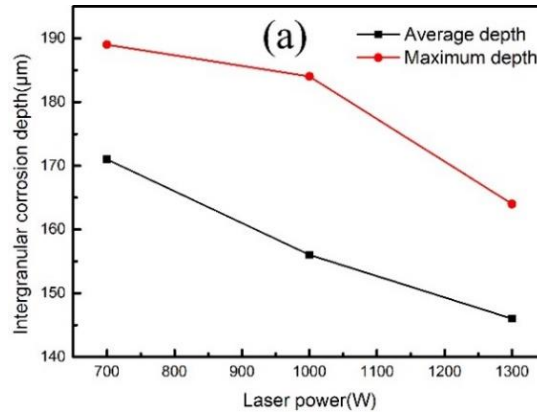| Laser power (W)	700	1000	1300
	157	142	147
Corrosion depth (μm)	189	184	127
	167	143	164
Average corrosion depth (μm)	171	156	146
Maximum corrosion depth (μm)	189	184	164

Figure 9. IGC depth in weld metals produced with different laser powers

Fig.9 is a line diagram of the IGC depth of the weld metals produced with different laser powers. With increasing laser power, the average IGC depth decreases gradually, from 171 μm (at 700 W) to 156 μm (at 1000 W). When the laser power continues to increase to 1300 W, the average IGC depth decreases to 146 μm. Similarly, the maximum IGC depth of the weld metal tends to decrease with increasing laser power. At 700 W, the maximum corrosion depth is 189 μm while it is 164 μm at 1300 W, The maximum corrosion depth decreases by approximately 13%. The analysis shows that with increasing laser power, the uniformity of the composition distribution increases and the driving force for the nucleation of the second phase at the solid-liquid interface decreases, so the second phase precipitated that precipitates at the grain boundaries decreases with increasing laser power. IGC mainly occurs along the grain boundaries. A decrease in the second phase in the grain boundary leads to a decrease in the corrosion rate. Xue, et al [26] also found that the depth of IGC was related to the amount of precipitates. Therefore, the average and maximum depth of the inter-granular corrosion of the welds decreases with increasing laser power.

4. CONCLUSIONS

(1) As the laser power increases, the microstructure of the weld coarsens, the amount of bright white and dark black precipitates decreases, the size of the precipitated phase increases and the distribution is nonuniform.

(2) Electrochemical tests show that among the weld metal, the corrosion resistance of the BM is the lowest, while that of the weld metal is the highest, and that of the HAZ is between that of the BM and the weld metals. As the laser power increases, the corrosion resistance of the weld metal increases.

(3) The results of the IGC of the welded joints show that among the weld metals, the HAZ has the best IGC resistance and the corrosion degree is low; The IGC of BM is more severe than that of HAZ, where the local corrosion is obvious. The weld metal is the most severely corroded, because the surface is covered with a large amount of white corrosion products.

(4) The IGC test in the weld metal shows that the average and maximum depth of IGC decreases with increasing laser power. When the laser power reaches 1300 W, the average and maximum depths are 146 μm and 164 μm, respectively.

References

1. R. J. Rioja, J. Liu, *Metallurgical and Materials Transactions*, 43 (2012) 3325.
2. N. Nayan, S. V. S. N. Murty, A. K. Jha, B. Pant, S. C. Sharma, K. M. George, *Materials Science and Engineering,* 576 (2013) 21.
3. J. Zhang, X. S. Feng, J. S. Gao, H. Huang, Z. Q. Ma, L. J. Guo, *Journal Of Materials Science & Technology,* 34 (2018) 219.
4. T. Dursun, C. Soutis, *Materials & Design*, 56 (2014) 862.
5. I. G. Solórzano, F. A. Darwish, M. C. de Macedo, S. O. de Menezes, *Materials Science and Engineering,* 348 (2003) 251.
6. M.S. han, S. J. Lee, J. Cheul, *Transactions of Nonferrous Metals Society of China*, 19 (2009) S17.
7. P. Cavaliere, M. Cabibbo, F. Panella, A. Squillace, *Materials & Design*, 30 (2009) 3622.
8. Y. Mei, L. Yang, Z. Junlei, X. Dong, Z. Zhimin, W. Dan, *Transactions of the Indian Institute of Metals*, 71 (2018) 2487.
9. P. Cavaliere, M. Cabibbo, F. Panella, A. Squillace, *Materials & Design*, 30 (2009) 3622.
10. A. Balbo, A. Frignani, V. Grassi, F. Zucchi, *Corrosion Science*, 73 (2013) 80.
11. W. Xu, J. Liu, *Corrosion Science*, 51 (2009) 2751.
12. E. Bousquet, M. Puiggali, O. Devos, M. Touzet, *Corrosion Science*, 53 (2011) 3034.
13. V. Proton, J. Alexis, E. Andrieu, *Journal Of The Electrochemical Society*, 158 (2011) C139.
14. F. Y. Shu, L. Wu, H. Y. Zhao, S. H. Sui, L. Zhou, J. Zhang, *Materials Letters*, 211 (2017) 235.
15. A. A. El-Aty, Y. Xu, X. Guo, S. Zhang, D. Chen, *Journal of Advanced Research*, 10 (2017) 49.
16. X. Zhang, T. Huang, W. Yang, R. Xiao, Z. Liu, L. Li, *Journal of Materials Processing Technology*, 237 (2016) 301.
17. X. J. Wang, T. Zhao, *Chinese Journal of Aeronautics*, 24(2011) 681.
18. L. I. Jin-Feng, W. J. Chen, X. S. Zhao, W. D. Ren, Z. Q. Zheng, *Transactions Of Nonferrous Metals Society of China*, 16 (2006) 1177.
19. F. Liu, X. Wang, B. Zhou, C. Huang, F. Lyu, *Materials*, 11(2018).
20. Y. Ma, X. Chen, X. Zhou, Y. Yi, Y. Liao, W. Huang, *Surface and Interface Analysis*, 48 (2016) 739.
21. Y. Ma, X. Zhou, Y. Liao, Y. Yi, H. Wu, Z. Wang, *Corrosion Science*, 107 (2016) 41.
22. Q. Liu, R. H. Zhu, D. Y. Liu, Y. Xu, J. F. Li, Y. L. Chen, *Materials & Corrosion*, 68 (2017).
23. O. Noémie, *Metallurgical and Materials Transactions*, 48 (2017) 51.
24. B. Decreus, A. Deschamps, P. Donnadieu, *Materials Science and Engineering*, 586 (2013) 418.
25. L Dong, J Schneider, *Journal of Materials Science*, 43(2008) 7445.

26. X. U. Yue, X.Wang, Z. Yan, L. I. Jiaxue, *Chinese Journal of Aeronautics*, 24 (2011) 681.